nanomaterials

MDPI

Article

Reset First Resistive Switching in $Ni_{1-x}O$ Thin Films as Charge Transfer Insulator Deposited by Reactive RF Magnetron Sputtering

Dae-woo Kim [1], Tae-ho Kim [1,2], Jae-yeon Kim [1] and Hyun-chul Sohn [1,*]

[1] Department of Materials Science and Engineering, Yonsei University, Seoul 03722, Korea; daewoo.kim@yonsei.ac.kr (D.-w.K.); kkthh22@yonsei.ac.kr (T.-h.K.); jaeyeonkim@yonsei.ac.kr (J.-y.K.)
[2] Lam Research, Daesan-ro 288, Icheon-si 17336, Korea
* Correspondence: hyunchul.sohn@yonsei.ac.kr; Tel.: +82-2-2123-5850

Abstract: Reset-first resistive random access memory (RRAM) devices were demonstrated for off-stoichiometric $Ni_{1-x}O$ thin films deposited using reactive sputtering with a high oxygen partial pressure. The $Ni_{1-x}O$ based RRAM devices exhibited both unipolar and bipolar resistive switching characteristics without an electroforming step. Auger electron spectroscopy showed nickel deficiency in the $Ni_{1-x}O$ films, and X-ray photoemission spectroscopy showed that the Ni^{3+} valence state in the $Ni_{1-x}O$ films increased with increasing oxygen partial pressure. Conductive atomic force microscopy showed that the conductivity of the $Ni_{1-x}O$ films increased with increasing oxygen partial pressure during deposition, possibly contributing to the reset-first switching of the $Ni_{1-x}O$ films.

Keywords: resistive random access memory; nickel oxide; nickel vacancy; reset-first resistive switching; oxygen partial pressure; conductivity; area dependence

Citation: Kim, D.-w.; Kim, T.-h.; Kim, J.-y.; Sohn, H.-c. Reset First Resistive Switching in $Ni_{1-x}O$ Thin Films as Charge Transfer Insulator Deposited by Reactive RF Magnetron Sputtering. *Nanomaterials* **2022**, *12*, 2231. https://doi.org/10.3390/nano12132231

Academic Editor: Seiichi Miyazaki

Received: 4 June 2022
Accepted: 27 June 2022
Published: 29 June 2022

1. Introduction

Resistive random access memory (RRAM) [1] has been widely studied as a candidate for next-generation non-volatile memory to overcome the limitations of conventional memories, such as flash memory and dynamic random access memory (DRAM). RRAM has a relatively low operation voltage with excellent program and erase speed [2]. In addition, the device could be fabricated in a simple metal–insulator–metal (MIM) [3] structure, enabling the high-density cell structure of a cross-bar array with $4F^2$ [4,5]. It was reported that numerous transition metal oxides, including Al_2O_3 [6,7], HfO_2 [8–10], NiO_x [11–14], TiO_x [15,16], TaO_x [17,18], Nb_2O_5 [19,20], and $Pr_{1-x}Ca_xMnO_3$ [21–23] show resistive switching (RS) characteristics. Moreover, various deposition techniques, such as sputtering [24–28], atomic layer deposition (ALD) [29] and pulsed laser deposition (PLD) [30] were used for the formation of such oxides. Notably, nickel oxide (NiO) film is one of the most widely studied oxides and is reported to have low operation power, a high on/off resistance ratio and is compatible with the CMOS fabrication process [31,32]. NiO has a rock salt structure composed of Ni^{2+} and O^{2-} and is a member of the strongly correlated 3d transition metal oxides that exhibit charge-transfer insulator behavior [33,34]. It is an insulating oxide with a wide bandgap ($E_g \approx 4.3$ eV) due to the charge transfer gap caused by "Hubbard U" between the 2p and 3d states [34,35]. Therefore, the pristine state of NiO is typically the insulating state in RRAM [36,37]. The RS phenomenon in NiO has been mainly described as the formation and rupture of conductive filaments. This reversible resistance transition between the high-resistance state (HRS) and low-resistance state (LRS) is caused by applying electrical stress after an "electroforming" step [38]. It was suggested that oxygen atoms are migrated by the electric field, leaving oxygen vacancies (V_o^{2+}) at the vacated sites during the electroforming step; the adjacent Ni^{2+} atoms are changed to Ni^0 to compensate for the charge state, resulting in a Ni filament [39–41]. The electroforming

process degrades the chemical and physical properties of devices of MIM structure, affecting their reliability. The characteristics of RS uniformity also deteriorate because of non-uniform filament formation among MIM devices [42]. Moreover, electroforming requires additional high-voltage circuits, significantly reducing the device density. Therefore, research on devices that can be operated without an electroforming step is essential for realizing RS memories [43–45].

This study investigated the RS characteristics of off-stoichiometric $Ni_{1-x}O$ films for unipolar and bipolar RSs (URS and BRS, respectively). Particularly, it was demonstrated that nickel-deficient $Ni_{1-x}O$ films deposited under excessive oxygen partial pressure exhibit a reset-first RS without an electroforming step. An RRAM device with a reset-first RS could be an alternative to overcome the limitations of RRAM requiring an electro-forming step.

2. Experimental

MIM devices with Pt/NiO/Pt and Pt/NiO/TiN stacks were fabricated for electrical characterization. First, Ti/TiN adhesive layers with thicknesses of 10–50 nm were deposited onto SiO_2 on a Si substrate using DC magnetron sputtering. Pt or TiN films were then deposited as bottom electrodes (BE). BE with various areas of 0.18~4.0 μm^2 were formed to investigate the area-dependence of the electrical characteristics. After BE formation, off-stoichiometric $Ni_{1-x}O$ films with a thickness of 10 nm were deposited via reactive RF magnetron sputtering using a Ni target under various O_2 partial pressures. During sputtering, the base and working pressures were less than 3×10^{-3} and 3 mTorr, respectively. During deposition, the RF power and temperature of the substrate were main-tained at 100 W and 400 °C, respectively. The fraction of the O_2 partial pressure in the mixture of Ar and O_2 varied from 10% to 50% for deposition. Finally, Pt top electrodes (TEs) with a thickness of 100 nm were formed using DC magnetron sputtering and a lift-off process. The electrical characteristics of the device were characterized using a Keysight B1500A analyzer at 21~23 °C. RS under DC bias was measured with a com-pliance current of 10 mA to avoid hard breakdown of the $Ni_{1-x}O$ films. The spatial distribution of conductivity in the pristine state was investigated using conductive atomic force microscopy (C-AFM) (Park Systems, XE-100) with a measurement bias of 3 V [46,47]. Grazing incidence X-ray diffraction (GI-XRD, Rigaku SmartLab), Auger electron spectroscopy (AES, PHI-700, ULVAC-PHI), and X-ray photoelectron spectroscopy (XPS, K-alpha, Thermo U. K.) analyses were conducted to investigate the crystallinity, composition, and valence states of Ni in the $Ni_{1-x}O$ films, respectively.

3. Results and Discussion

XRD analysis was conducted to investigate the crystallinity of $Ni_{1-x}O$ films. The XRD patterns of $Ni_{1-x}O$ films deposited under various O_2 fractions are illustrated in Figure 1a. The peaks of NiO (111), NiO (200), NiO (220), and NiO (311) imply a polycrystalline structure [48]. NiO films, deposited with an O_2 partial pressure fraction of 50% showed lower intensity with a more comprehensive full-width half maximum (FWHM), implying poorer crystallinity of NiO films. The XRD peak of the (111) plane shifted to lower diffraction with increasing O_2 partial pressure, indicating an increase in the lattice constant with increasing O_2 partial pressure, as shown in Figure 1b. The increase in the lattice constant could be ascribed to the increased strain effect as Ni vacancies increase with excessive O_2 partial pressure [48–50]. Figure 1c shows the composition of Ni and O, estimated from AES analysis of the $Ni_{1-x}O$ films with various O_2 partial pressures during deposition. The volume of Ni is gradually reduced with increasing O_2 partial pressure, resulting in a Ni-deficient $Ni_{1-x}O$ film. The compositions of nickel oxide at 10% and 50% O_2 partial pressures were estimated to be $Ni_{0.89}O$ and $Ni_{0.86}O$, respectively.

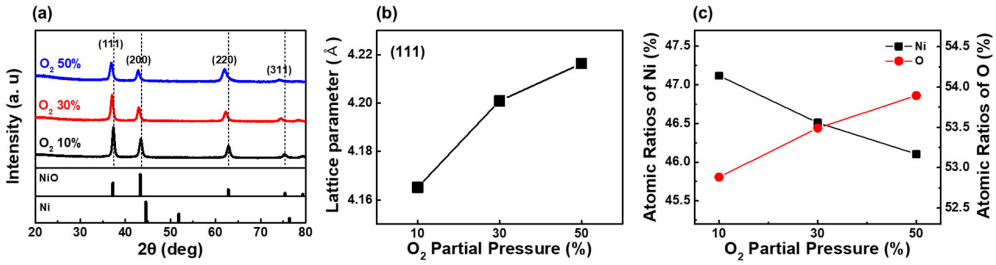

Figure 1. (**a**) XRD patterns of $Ni_{1-x}O$ films deposited with various oxygen partial pressures. (**b**) Lattice constant of $Ni_{1-x}O$, estimated from (111) peak position, as a function of oxygen partial pressures. (**c**) Nickel and oxygen composition in $Ni_{1-x}O$ by AES.

Figure 2a shows the typical behavior of $Pt/Ni_{1-x}O/Pt$ stacks. The pristine $Ni_{1-x}O$ films deposited under an O_2 partial pressure fraction of 10% offered an initial high resistivity [51] at an applied voltage of 1.77 V (1.4 MV/cm) on the TE. The film resistance changed from HRS to LRS during the forming step. The resistance state was changed back to HRS at 0.64 V (0.5 MV/cm) during the subsequent bias application, exhibiting reversible switching for the positive bias on TE. The difference between the forming voltage (V_{form}) and set voltage (V_{set}) was approximately 0.57 V. In contrast, pristine $Ni_{1-x}O$ films deposited under the 30% or 50% O_2 ratio showed low resistance in the pristine state without the electroforming step and reset-first RS behavior, where the initial LRS state was changed to the HRS state, as shown in Figure 2b,c. While V_{set} is similar to that of $Ni_{1-x}O$ films for the O_2 partial pressure fraction of 10%, the I_{HRS}/I_{LRS} ratio decreased because of the overall high current level in the HRS state. In particular, the I_{HRS} between these oxygen partial pressure fractions showed that the 50% O_2 ratio was 10 times higher than that of 30% O_2. The I-V curves of $TiN/Ni_{1-x}O/Pt$ stacks are plotted in Figure 2d–f. The $Ni_{1-x}O$ film deposited under a 10% O_2 partial pressure fraction show BRS [52] characteristics, as shown in Figure 2d. The pristine $Ni_{1-x}O$ film showed high resistivity, and the resistance state changed to LRS after the electroforming step with a negative bias on TE. The difference between V_{form} (−4.0 V) and V_{set} (−0.7 V) was approximately 3.3 V. On the contrary, the $Ni_{1-x}O$ film deposited under the 30% or 50% O_2 partial pressure fraction showed reset-first BRS behavior for a positive voltage on the TE, as shown in Figure 2e,f.

Figure 3 shows the electric currents at 0.64 V of the $Pt/Ni_{1-x}O/TiN$ stacks in the LRS and HRS states, where $Ni_{1-x}O$ films were deposited at various O_2 partial pressures. The mean values of I_{HRS} and I_{LRS} (red line) increased with the O_2 ratio, suggesting that the $Ni_{1-x}O$ film conductivity depends on the O_2 partial pressure, as shown in Figure 3a. The $Ni_{1-x}O$ films with a 10% O_2 fraction required electroforming for resistive switching, but the $Ni_{1-x}O$ films with a 30% O_2 fraction or higher showed reset-first RS behavior without electroforming. Figure 3b shows the electrical currents at 0.64 V in the LRS states, which has a similar tendency to the I_{HRS} with O_2 partial pressure, but the slope was lower than that of the I_{HRS} state. The I_{HRS} and I_{LRS} showed the highest values for $Ni_{1-x}O$ films deposited under the 50% O_2 partial pressure fraction.

To understand the nature of resistance switching, HRS and LRS resistances were measured from devices with BE of 0.18, 0.38, 2.00, and 3.69 μm^2 at a bias of ±0.48 V. Figure 4a shows the area dependent resistance for BRS device with $Ni_{1-x}O$ films deposited by 10% O_2 partial pressure fraction. The resistance of the HRS remained almost constant with decreasing geometric device area, while that of the LRS is almost independent of the device area. These area-independent characteristics imply that resistance switching through the device occurs in local regions, such as filament paths, rather than homogeneously distributed switching paths [53–57]. Meanwhile, the resistances of reset-first RS devices with $Ni_{1-x}O$ films deposited at 50% O_2 partial pressure showed increased dependence on the device area, as shown in Figure 4b. Because the area dependence of the LRS for $Ni_{1-x}O$ films with 50% O_2 partial pressure is close to that of $Ni_{1-x}O$ films with 10% O_2 partial pressure, the nature of the RS is filamentary in the local area. The significant dependence

of HRS on the $Ni_{1-x}O$ films with 50% O_2 partial pressure is attributed to the reduced resistance of the $Ni_{1-x}O$ films, as shown in Figure 4b.

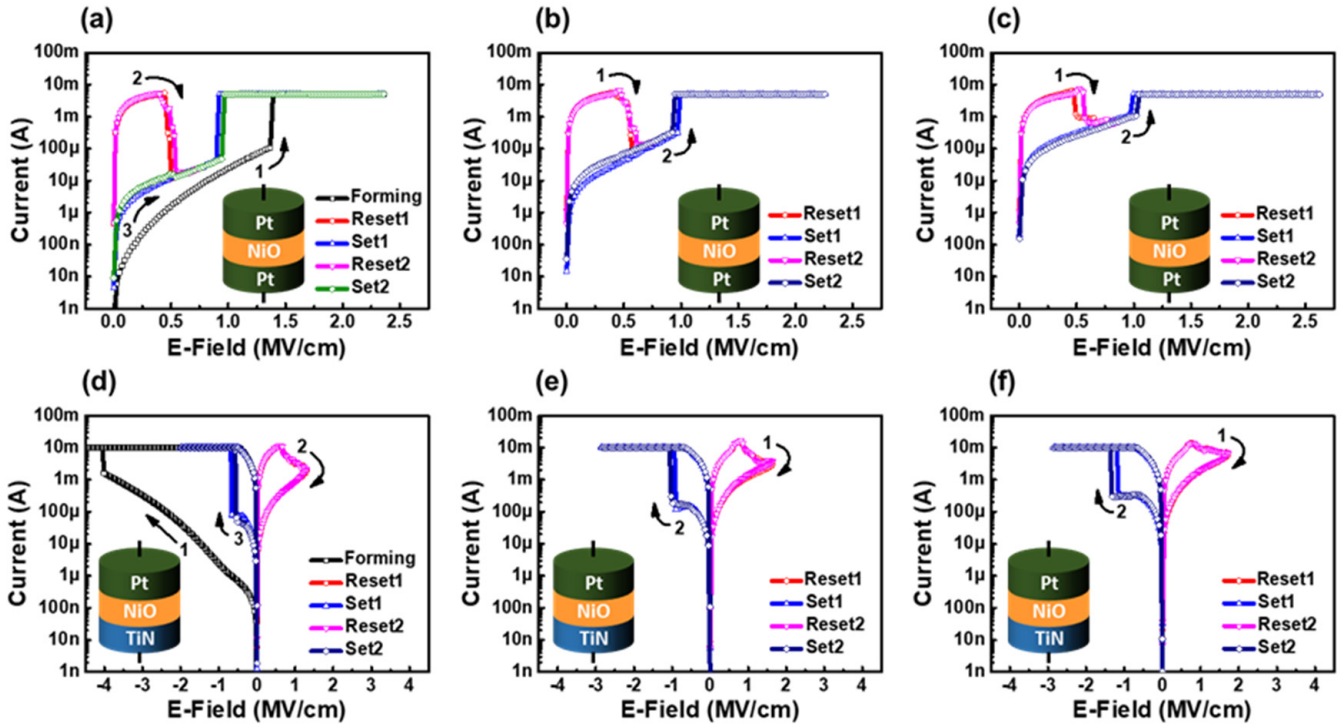

Figure 2. I−V characteristics of $Ni_{1-x}O$ devices with a bottom electrode of 2 × 2 μm^2. URS characteristics of $Ni_{1-x}O$ films deposited with partial oxygen pressure of (**a**) 10%, (**b**) 30% and (**c**) 50%. BRS characteristics of $Ni_{1-x}O$ films deposited with oxygen partial pressure fraction of (**d**) 10%, (**e**) 30% and (**f**) 50%.

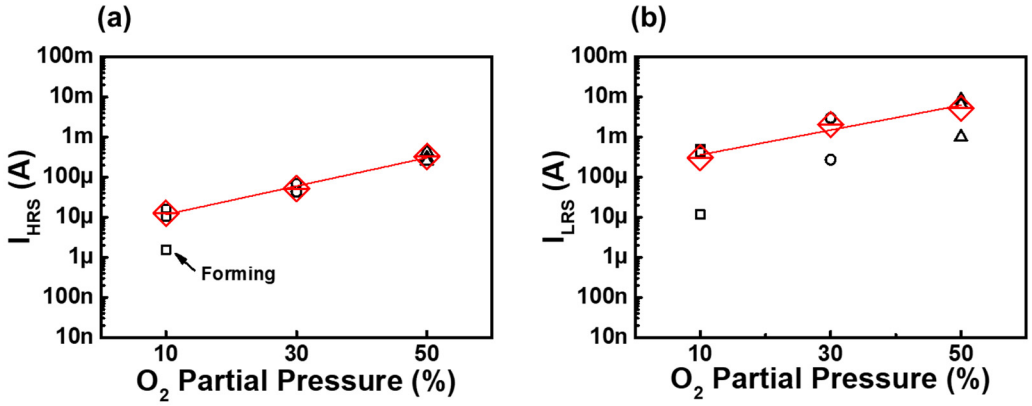

Figure 3. Influence of oxygen partial pressure on (**a**) I_{HRS} of $Ni_{1-x}O$ films and (**b**) I_{LRS} of $Ni_{1-x}O$ films.

The DC, and AC endurance characteristics of the $Ni_{1-x}O$ device are shown in Figure S1. DC endurance in Figure S1a was measured at a read voltage (V_{read}) of ±0.25 V under a compliance current of 10 mA. The measured I_{HRS}/I_{LRS} ratio is higher than 10^1 even after 10^3 cycles. Figure S1b shows the AC endurance under pulse, which is measured with a set pulse of −0.95 V with 180 ns, a reset pulse of 1.2 V with 180 ns, and a V_{read} of 0.3 V conditions. The device has a uniform I_{HRS}/I_{LRS} ratio even after 10^5 cycles, which results in a stable RS property.

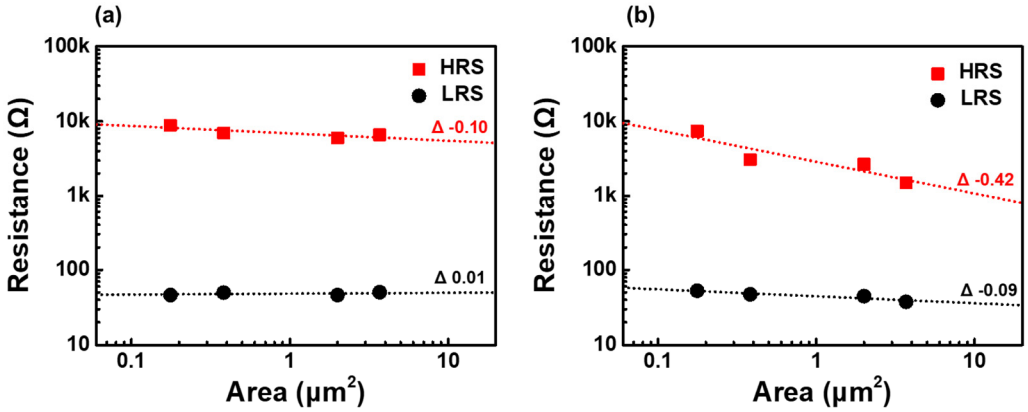

Figure 4. Area dependence of HRS and LRS resistances for Pt/$Ni_{1-x}O$/TiN stacks (**a**) with $Ni_{1-x}O$ films, deposited with oxygen partial pressure fraction of 10%, with electroforming (**b**) with $Ni_{1-x}O$ films that are deposited with oxygen partial pressure fraction of 50%, with reset-first BRS without electroforming.

C-AFM measurements investigated the two-dimensional (2D) variation of the $Ni_{1-x}O$ film conductivity. Figure 5a illustrates the scheme of the C-AFM measurement. NiO/Pt and NiO/SiO_2/Pt stacks were simultaneously formed on a sample to compare the differences during the current image mapping. Cross-sectional TEM images of the $Ni_{1-x}O$ films for C-AFM measurements are shown in Figure 5b. The sample-to-sample variation in the $Ni_{1-x}O$ thickness on the SiO_2/Pt stacks was estimated to be within 15%. Therefore, we ignore the difference in conductivity due to thickness variation. Figure 5c–e show the current mapping images at a bias of 3 V from $Ni_{1-x}O$ films deposited under various O_2 partial pressures. The left region of each mapping image represents the reference of the insulating SiO_2 between the BEs and $Ni_{1-x}O$ films. The regions on the right represent the $Ni_{1-x}O$ films on the Pt BEs in their pristine state. Similar to the I-V characteristics of MIM devices, C-AFM showed an increased current through the $Ni_{1-x}O$ films with increasing O_2 partial pressure. The conductive regions in the $Ni_{1-x}O$ film regions increased with increasing O_2 partial pressure fraction, as shown in Figure 5d,e. In particular, the current distribution is relatively uniform in $Ni_{1-x}O$ film with a 50% O_2 fraction. In contrast, films deposited under 10% O_2 partial pressure fraction showed improved resistivity, as shown in Figure 5c.

The effect of the O_2 partial pressure on the chemical bonding states in the $Ni_{1-x}O$ films is investigated through XPS analysis. Figure 6a–c show the Ni $2p_{3/2}$ peaks of $Ni_{1-x}O$ films deposited with various O_2 partial pressures. Ni^0, Ni^{2+} and Ni^{3+} states with binding energies of 852.5, 853.7, and 855.5 eV, respectively, are used for deconvolution of Ni $2p_{3/2}$ peaks [58,59].

The proportion of the Ni^{3+} state was estimated from the ratio of the Ni^{3+} peak area to the Ni^{2+} peak area. The Ni^{3+} valence state increased while the fraction of Ni^{2+} ions decreased with increasing O_2 partial pressure (Figure 6a–c). The Ni^{3+} ratio in the film grown under 10% and 50% O_2 partial pressure was estimated at 14.0% and 23.9%, respectively. Meanwhile, the Ni^0 state at the 852.5 eV peak was not observed in our Ni $2p_{2/3}$ peak analysis, although it was considered a conductive path in previous studies [39–41]. Conventionally, Ni vacancies form in Ni-deficient NiO films with relatively excessive oxygen. It was reported that nickel deficiency could promote the further oxidation of Ni^{2+} ions, which can be expressed with Kröger–Vink notation, as follows [48,49]:

$$2Ni_{Ni}^{x} + \frac{1}{2}O_2(g) \rightarrow 2Ni_{Ni}^{\bullet} + O_o^x + V_{Ni}^{''}, \quad (1)$$

where Ni_{Ni}^{x}, $Ni_{Ni}^{\bullet}$, O_o^x, $V_{Ni}^{''}$ represent Ni^{2+}, Ni^{3+}, O^{2-}, and ionized Ni vacancies, respectively. Ni^{2+} ions react with oxygen to generate ionized nickel vacancies and two Ni^{3+} ions, which affect the conductivity of the nickel oxide films. Therefore, it is shown that the increase

in Ni^{3+} in $Ni_{1-x}O$ films is related to the increase in the current in the HRS state of MIM devices and C-AFM. It is expected that Ni deficiency in $Ni_{1-x}O$ films grown under high O_2 partial pressure causes a high Ni^{3+} concentration, leading to a highly conductive state and possibly the reset-first RS behavior with reinforced localized conductive paths [39,60,61]. Further investigation is required to understand how excess Ni^{3+} ions produce the reset-first resistive switching behavior in $Ni_{1-x}O$ films.

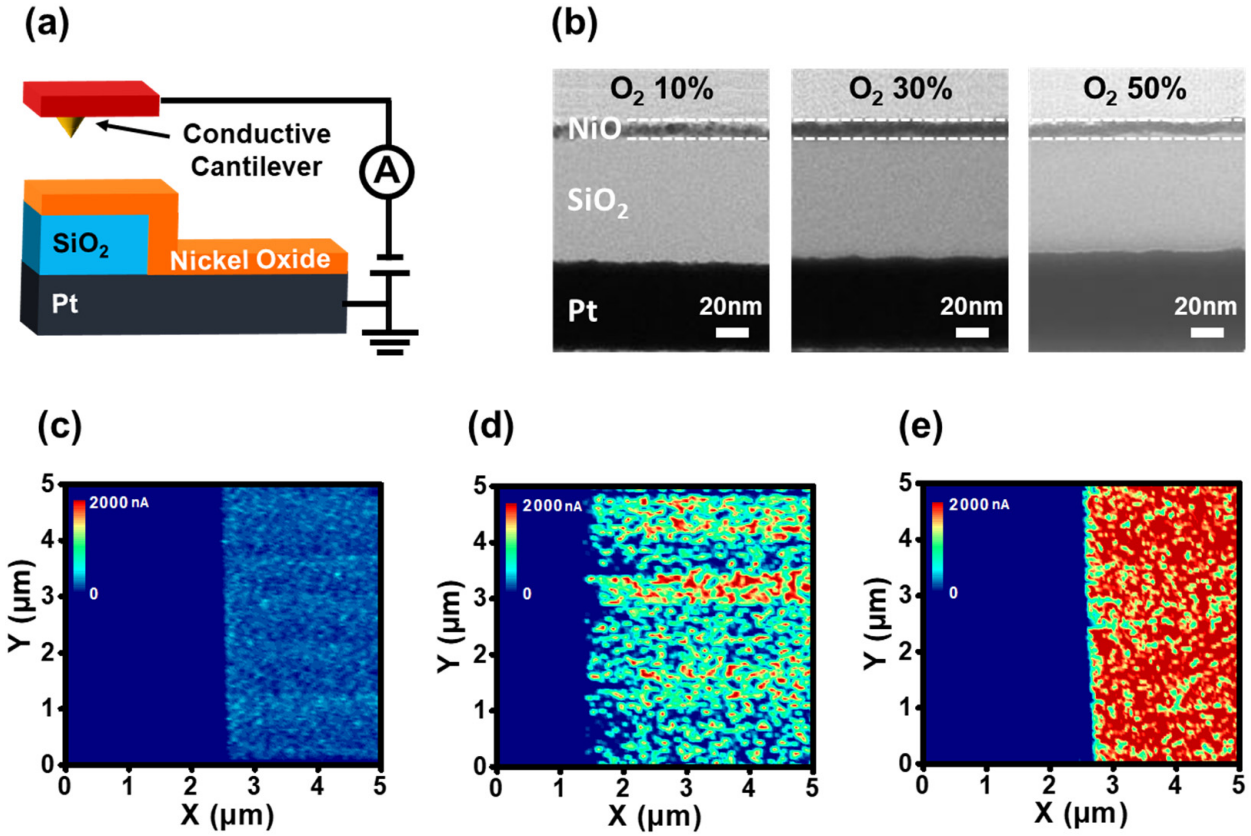

Figure 5. (**a**) Schematic diagram of the C-AFM measurement. (**b**) Cross-sectional TEM image of $Ni_{1-x}O$ films deposited at various oxygen partial pressure. C-AFM current mapping images of the pristine $Ni_{1-x}O$ films under oxygen partial pressure fraction of (**c**) 10%, (**d**) 30%, and (**e**) 50%.

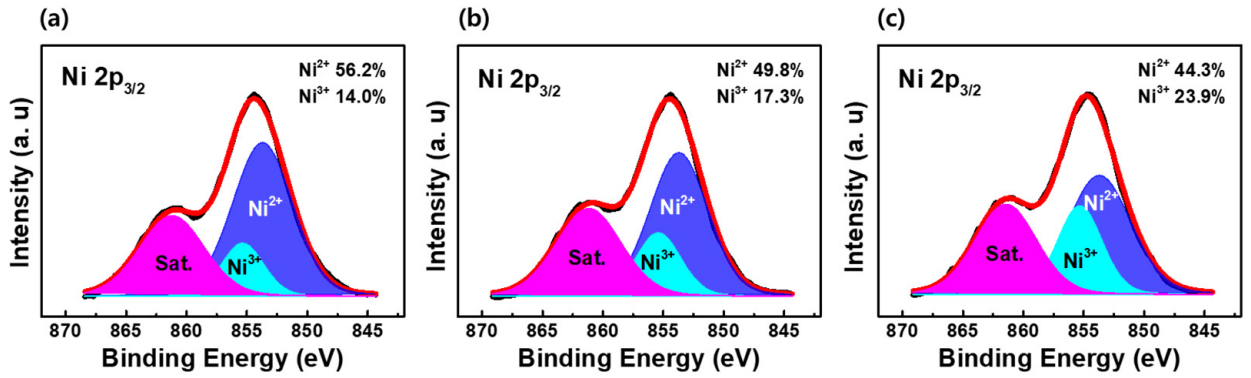

Figure 6. XPS peaks of Ni $2p_{3/2}$ of $Ni_{1-x}O$ films with oxygen partial pressure fraction of (**a**) 10% (**b**) 30% (**c**) 50%.

4. Conclusions

In this study, the reset-first RS characteristics of off-stoichiometric $Ni_{1-x}O$ films were investigated. The RS behavior without the electroforming step was observed in the unipolar

and bipolar off-stoichiometric $Ni_{1-x}O$ films. Ni^{3+} distribution contributes significantly to the conductivity of the pristine $Ni_{1-x}O$ films. The conductivity and Ni deficiency of pristine $Ni_{1-x}O$ films increased as the O_2 partial pressure increased during a deposition as revealed by the C-AFM and AES results. Moreover, Ni^{2+} was further oxidized to Ni^{3+} as the O_2 partial pressure increased, as revealed by the XPS results.

The Ni_2O_3 bonding by Ni^{3+} ions is related to the reset-first RS behavior without the electroforming step. This is advantageous in terms of device scale-down, making $Ni_{1-x}O$ films promising candidates for memory applications by overcoming the limitations of the electroforming step in RRAM.

Supplementary Materials: The following supporting information can be downloaded at: https://www.mdpi.com/article/10.3390/nano12132231/s1, Figure S1: Endurance characteristics of $Ni_{1-x}O$ bipolar RS device.

Author Contributions: Conceptualization, D.-w.K.; methodology, J.-y.K.; validation, D.-w.K., T.-h.K. and J.-y.K.; writing—original draft preparation, D.-w.K.; writing—review and editing, H.-c.S.; supervision, H.-c.S. All authors have read and agreed to the published version of the manuscript.

Funding: This work was supported by the Ministry of Trade, Industry and Energy, Korea under the Industrial Strategic Technology Development Program (Grant no. 100680075).

Conflicts of Interest: The authors declare no conflict of interest.

References

1. Zahoor, F.; Zulkifli, T.Z.A.; Khanday, F.A. Resistive Random access Memory (RRAM): An Overview of Materials, Switching Mechanism, Performance, Multilevel Cell (mlc) Storage, Modeling, and Applications. *Nanoscale Res. Lett.* **2020**, *15*, 90. [CrossRef] [PubMed]
2. Wang, H.; Yan, X. Overview of Resistive Random access Memory (RRAM): Materials, Filament Mechanisms, Performance Optimization, and Prospects. *Phys. Status Solidi (RRL)–Rapid Res. Lett.* **2019**, *13*, 1900073. [CrossRef]
3. Wang, L.; Yang, C.; Wen, J.; Gai, S. Emerging Nonvolatile Memories to Go Beyond Scaling Limits of Conventional CMOS Nanodevices. *J. Nanomater.* **2014**, *2014*, 927696. [CrossRef]
4. Pan, F.; Gao, S.; Chen, C.; Song, C.; Zeng, F. Recent progress in resistive random access memories: Materials, switching mechanisms, and performance. *Mater. Sci. Eng.: R: Rep.* **2014**, *83*, 1–59. [CrossRef]
5. Wong, H.S.P.; Lee, H.-Y.; Yu, S.; Chen, Y.-S.; Wu, Y.; Chen, P.-S.; Lee, B.; Chen, F.T.; Tsai, M.-J. Metal–Oxide RRAM. *Proc. IEEE* **2012**, *100*, 1951–1970. [CrossRef]
6. Quan, X.-T.; Zhu, H.-C.; Cai, H.-T.; Zhang, J.-Q.; Wang, X.-J. Resistive Switching Behavior in Amorphous Aluminum Oxide Film Grown by Chemical Vapor Deposition. *Chin. Phys. Lett.* **2014**, *31*, 078101. [CrossRef]
7. Rodrigues, A.; Santos, Y.; Rodrigues, C.; Macêdo, M. Al2O3 thin film multilayer structure for application in RRAM devices. *Solid-State Electron.* **2018**, *149*, 1–5. [CrossRef]
8. Lin, Y.S.; Zeng, F.; Tang, S.G.; Liu, H.Y.; Chen, C.; Gao, S.; Wang, Y.G.; Pan, F. Resistive switching mechanisms relating to oxygen vacancies migration in both interfaces in Ti/HfO_x/Pt memory devices. *J. Appl. Phys.* **2013**, *113*, 064510. [CrossRef]
9. Raghavan, N.; Fantini, A.; Degraeve, R.; Roussel, P.; Goux, L.; Govoreanu, B.; Wouters, D.; Groeseneken, G.; Jurczak, M. Statistical insight into controlled forming and forming free stacks for HfOx RRAM. *Microelectron. Eng.* **2013**, *109*, 177–181. [CrossRef]
10. Ku, B.; Abbas, Y.; Sokolov, A.S.; Choi, C. Interface engineering of ALD HfO2-based RRAM with Ar plasma treatment for reliable and uniform switching behaviors. *J. Alloy. Compd.* **2018**, *735*, 1181–1188. [CrossRef]
11. Seo, S.; Lee, M.-J.; Seo, D.H.; Jeoung, E.J.; Suh, D.-S.; Joung, Y.S.; Yoo, I.K.; Hwang, I.R.; Kim, S.H.; Byun, I.S.; et al. Reproducible resistance switching in polycrystalline NiO films. *Appl. Phys. Lett.* **2004**, *85*, 5655–5657. [CrossRef]
12. Yoshida, C.; Kinoshita, K.; Yamasaki, T.; Sugiyama, Y. Direct observation of oxygen movement during resistance switching in NiO/Pt film. *Appl. Phys. Lett.* **2008**, *93*, 042106. [CrossRef]
13. Liu, C.-Y.; Ho, J.-Y.; Huang, J.-J.; Wang, H.-Y. Transient Current of Resistive Switching of a NiO$_{x}$ Resistive Memory. *Jpn. J. Appl. Phys.* **2012**, *51*, 041101. [CrossRef]
14. Alagoz, H.S.; Tan, L.; Jung, J.; Chow, K.H. Switching characteristics of NiOx crossbar arrays driven by low-temperature electroforming. *Appl. Phys. A* **2021**, *127*, 499. [CrossRef]
15. Yang, J.J.; Inoue, I.H.; Mikolajick, T.; Hwang, C.S. Metal oxide memories based on thermochemical and valence change mechanisms. *MRS Bull.* **2012**, *37*, 131–137. [CrossRef]
16. Trapatseli, M.; Khiat, A.; Cortese, S.; Serb, A.; Carta, D.; Prodromakis, T. Engineering the switching dynamics of TiOx-based RRAM with Al doping. *J. Appl. Phys.* **2016**, *120*, 025108. [CrossRef]
17. Chen, C.; Song, C.; Yang, J.; Zeng, F.; Pan, F. Oxygen migration induced resistive switching effect and its thermal stability in W/TaO_x/Pt structure. *Appl. Phys. Lett.* **2012**, *100*, 253509. [CrossRef]

18. Jiang, Y.; Tan, C.C.; Li, M.H.; Fang, Z.; Weng, B.B.; He, W.; Zhuo, V.Y.-Q. Forming-Free TaOxBased RRAM Device with Low Operating Voltage and High On/Off Characteristics. *ECS J. Solid State Sci. Technol.* **2015**, *4*, N137–N140. [CrossRef]
19. Hanzig, F.; Mähne, H.; Veselý, J.; Wylezich, H.; Slesazeck, S.; Leuteritz, A.; Zschornak, M.; Motylenko, M.; Klemm, V.; Mikolajick, T.; et al. Effect of the stoichiometry of niobium oxide on the resistive switching of Nb 2 O 5 based metal–insulator–metal stacks. *J. Electron Spectrosc. Relat. Phenom.* **2015**, *202*, 122–127. [CrossRef]
20. Kundozerova, T.V.; Grishin, A.M.; Stefanovich, G.B.; Velichko, A.A. Anodic Nb2O5 Nonvolatile RRAM. *IEEE Trans. Electron Devices* **2012**, *59*, 1144–1148. [CrossRef]
21. Asamitsu, A.; Tomioka, Y.; Kuwahara, H.; Tokura, Y. Current switching of resistive states in magnetoresistive manganites. *Nature* **1997**, *388*, 50–52. [CrossRef]
22. Lashkare, S.; Chouhan, S.; Chavan, T.; Bhat, A.; Kumbhare, P.; Ganguly, U. PCMO RRAM for Integrate-and-Fire Neuron in Spiking Neural Networks. *IEEE Electron Device Lett.* **2018**, *39*, 484–487. [CrossRef]
23. Panwar, N.; Ganguly, U. Variability assessment and mitigation by predictive programming in Pr 0.7 Ca 0.3 MnO 3 based RRAM. In Proceedings of the 2015 73rd Annual Device Research Conference (DRC), Columbus, OH, USA, 21–24 June 2015; pp. 141–142.
24. Depla, D.; Mahieu, S. *Reactive Sputter Deposition*; Springer: Berlin/Heidelberg, Germany, 2008.
25. Stognij, A.; Sharko, S.; Serokurova, A.; Trukhanov, S.; Panina, L.; Ketsko, V.; Dyakonov, V.; Szymczak, H.; Vinnik, D.; Gudkova, S. Preparation and investigation of the magnetoelectric properties in layered cermet structures. *Ceram. Int.* **2019**, *45*, 13030–13036. [CrossRef]
26. Sharko, S.A.; Serokurova, A.I.; Novitskii, N.N.; Ketsko, V.A.; Smirnova, M.N.; Almuqrin, A.H.; Sayyed, M.I.; Trukhanov, S.V.; Trukhanov, A.V. A New Approach to the Formation of Nanosized Gold and Beryllium Films by Ion-Beam Sputtering Deposition. *Nanomaterials* **2022**, *12*, 470. [CrossRef]
27. Zubar, T.; Fedosyuk, V.; Tishkevich, D.; Kanafyev, O.; Astapovich, K.; Kozlovskiy, A.; Zdorovets, M.; Vinnik, D.; Gudkova, S.; Kaniukov, E.; et al. The Effect of Heat Treatment on the Microstructure and Mechanical Properties of 2D Nanostructured Au/NiFe System. *Nanomaterials* **2020**, *10*, 1077. [CrossRef]
28. Zubar, T.I.; Fedosyuk, V.M.; Trukhanov, S.V.; Tishkevich, D.I.; Michels, D.; Lyakhov, D.; Trukhanov, A.V. Method of surface energy investigation by lateral AFM: Application to control growth mechanism of nanostructured NiFe films. *Sci. Rep.* **2020**, *10*, 14411. [CrossRef]
29. George, S.M. Atomic Layer Deposition: An Overview. *Chem. Rev.* **2009**, *110*, 111–131. [CrossRef]
30. Greer, J.A. History and current status of commercial pulsed laser deposition equipment. *J. Phys. D Appl. Phys.* **2013**, *47*, 34005. [CrossRef]
31. Trukhanov, S.V.; Vasil'Ev, A.N.; Maignan, A.; Szymczak, H. Critical behavior of La0.825Sr0.175MnO2.912 anion-deficient manganite in the magnetic phase transition region. *J. Exp. Theor. Phys. Lett.* **2007**, *85*, 507–512. [CrossRef]
32. Trukhanov, A.; Kostishyn, V.; Panina, L.; Korovushkin, V.; Turchenko, V.; Vinnik, D.; Yakovenko, E.; Zagorodnii, V.; Launetz, V.; Oliynyk, V.; et al. Correlation of the atomic structure, magnetic properties and microwave characteristics in substituted hexagonal ferrites. *J. Magn. Magn. Mater.* **2018**, *462*, 127–135. [CrossRef]
33. Hüfner, S. Electronic structure of NiO and related 3d-transition-metal compounds. *Adv. Phys.* **1994**, *43*, 183–356. [CrossRef]
34. Ferreira, L.G.; Marques, L.K.T. Band structure of NiO revisited. *Mater. Sci. (Cond.-Mat. Mtrl.-Sci.)* **2009**. Available online: https://www.semanticscholar.org/paper/Band-structure-of-NiO-revisited-Ferreira-Teles/0d15b06260c2aff5df1c9531066bdac6f50f9145 (accessed on 26 June 2022).
35. Janod, E.; Tranchant, J.; Corraze, B.; Querré, M.; Stoliar, P.; Rozenberg, M.; Cren, T.; Roditchev, D.; Phuoc, V.T.; Besland, M.-P.; et al. Resistive Switching in Mott Insulators and Correlated Systems. *Adv. Funct. Mater.* **2015**, *25*, 6287–6305. [CrossRef]
36. Karolak, M.; Ulm, G.; Wehling, T.; Mazurenko, V.; Poteryaev, A.; Lichtenstein, A. Double counting in LDA+DMFT—The example of NiO. *J. Electron Spectrosc. Relat. Phenom.* **2010**, *181*, 11–15. [CrossRef]
37. Xue, K.-H.; de Araujo, C.A.P.; Celinska, J.; McWilliams, C. A non-filamentary model for unipolar switching transition metal oxide resistance random access memories. *J. Appl. Phys.* **2011**, *109*, 091602. [CrossRef]
38. Xu, N.; Liu, L.; Sun, X.; Liu, X.; Han, D.; Wang, Y.; Han, R.; Kang, J.; Yu, B. Characteristics and mechanism of conduction/set process in TiN/ZnO/Pt resistance switching random-access memories. *Appl. Phys. Lett.* **2008**, *92*, 232112. [CrossRef]
39. Chien, F.S.-S.; Wu, Y.T.; Lai, G.L.; Lai, Y.H. Disproportionation and comproportionation reactions of resistive switching in polycrystalline NiOx films. *Appl. Phys. Lett.* **2011**, *98*, 153513. [CrossRef]
40. Russo, U.; Ielmini, D.; Cagli, C.; Lacaita, A.L. Filament Conduction and Reset Mechanism in NiO-Based Resistive-Switching Memory (RRAM) Devices. *IEEE Trans. Electron Devices* **2009**, *56*, 186–192. [CrossRef]
41. Chen, Y.S.; Kang, J.F.; Chen, B.; Gao, B.; Liu, L.F.; Liu, X.Y.; Wang, Y.Y.; Wu, L.; Yu, H.Y.; Wang, J.Y.; et al. Microscopic mechanism for unipolar resistive switching behaviour of nickel oxides. *J. Phys. D Appl. Phys.* **2012**, *45*, 65303. [CrossRef]
42. Grossi, A.; Nowak, E.; Zambelli, C.; Pellissier, C.; Bernasconi, S.; Cibrario, G.; el Hajjam, K.; Crochemore, R.; Nodin, J.; Olivo, P. Fundamental variability limits of filament-based RRAM. In Proceedings of the 2016 IEEE International Electron Devices Meeting (IEDM), San Francisco, CA, USA, 3–7 December 2016; pp. 4.7.1–4.7.4.
43. Fang, Z.; Yu, H.Y.; Li, X.; Singh, N.; Lo, G.Q.; Kwong, D.L. HfOx/TiOx/HfOx/TiOx Multilayer-Based Forming-Free RRAM Devices With Excellent Uniformity. *IEEE Electron Device Lett.* **2011**, *32*, 566–568. [CrossRef]
44. Luo, Q.; Zhang, X.; Hu, Y.; Gong, T.; Xu, X.; Yuan, P.; Ma, H.; Dong, D.; Lv, H.; Long, S.; et al. Self-Rectifying and Forming-Free Resistive-Switching Device for Embedded Memory Application. *IEEE Electron Device Lett.* **2018**, *39*, 664–667. [CrossRef]

45. Aglieri, V.; Lullo, G.; Mosca, M.; Macaluso, R.; Zaffora, A.; DI Franco, F.; Santamaria, M.; Cicero, U.L.; Razzari, L. Forming-Free and Self-Rectifying Resistive Switching Effect in Anodic Titanium Dioxide-Based Memristors. In Proceedings of the 2018 IEEE 4th International Forum on Research and Technology for Society and Industry (RTSI), Palermo, Italy, 10–13 September 2018; pp. 1–4. [CrossRef]
46. De Wolf, P.; Snauwaert, J.; Clarysse, T.; Vandervorst, W.; Hellemans, L. Characterization of a point-contact on silicon using force microscopy-supported resistance measurements. *Appl. Phys. Lett.* **1995**, *66*, 1530–1532. [CrossRef]
47. Alexeev, A.; Loos, J.; Koetse, M. Nanoscale electrical characterization of semiconducting polymer blends by conductive atomic force microscopy (C-AFM). *Ultramicroscopy* **2006**, *106*, 191–199. [CrossRef] [PubMed]
48. Kim, D.S.; Lee, H.C. Nickel vacancy behavior in the electrical conductance of nonstoichiometric nickel oxide film. *J. Appl. Phys.* **2012**, *112*, 034504. [CrossRef]
49. Chen, T.; Wang, A.; Shang, B.; Wu, Z.; Li, Y.; Wang, Y. Property modulation of NiO films grown by radio frequency magnetron sputtering. *J. Alloy. Compd.* **2015**, *643*, 167–173. [CrossRef]
50. Jang, W.-L.; Lu, Y.-M.; Hwang, W.-S.; Hsiung, T.-L.; Wang, H.P. Point defects in sputtered NiO films. *Appl. Phys. Lett.* **2009**, *94*, 062103. [CrossRef]
51. Lombardo, S.; Stathis, J.H.; Linder, B.P.; Pey, K.L.; Palumbo, F.; Tung, C.H. Dielectric breakdown mechanisms in gate oxides. *J. Appl. Phys.* **2005**, *98*, 121301. [CrossRef]
52. Akinaga, H.; Shima, H. Resistive Random Access Memory (ReRAM) Based on Metal Oxides. *Proc. IEEE* **2010**, *98*, 2237–2251. [CrossRef]
53. Liu, L.; Hou, Y.; Chen, B.; Gao, B.; Kang, J. Improved unipolar resistive switching characteristics of mixed-NiOx/NiOy-film-based resistive switching memory devices. *Jpn. J. Appl. Phys.* **2015**, *54*, 094201. [CrossRef]
54. Das, N.C.; Kim, M.; Rani, J.R.; Hong, S.-M.; Jang, J.-H. Electroforming-Free Bipolar Resistive Switching Memory Based on Magnesium Fluoride. *Micromachines* **2021**, *12*, 1049. [CrossRef]
55. Das, N.C.; Oh, S.-I.; Rani, J.R.; Hong, S.-M.; Jang, J.-H. Multilevel Bipolar Electroforming-Free Resistive Switching Memory Based on Silicon Oxynitride. *Appl. Sci.* **2020**, *10*, 3506. [CrossRef]
56. Li, Y.-T.; Long, S.-B.; Lü, H.-B.; Liu, Q.; Wang, Q.; Wang, Y.; Zhang, S.; Lian, W.-T.; Liu, S.; Liu, M. Investigation of resistive switching behaviours in WO3-based RRAM devices. *Chin. Phys. B* **2011**, *20*, 017305. [CrossRef]
57. Lee, J.; Park, J.; Jung, S.; Hwang, H. Scaling effect of device area and film thickness on electrical and reliability characteristics of RRAM. In Proceedings of the 2011 IEEE International Interconnect Technology Conference, Dresden, Germany, 8–12 May 2011; pp. 1–3.
58. Park, C.; Kim, J.; Lee, K.; Oh, S.K.; Kang, H.J.; Park, N.S. Electronic, Optical and Electrical Properties of Nickel Oxide Thin Films Grown by RF Magnetron Sputtering. *Appl. Sci. Converg. Technol.* **2015**, *24*, 72–76. [CrossRef]
59. Grosvenor, A.P.; Biesinger, M.C.; Smart, R.S.C.; McIntyre, N.S. New interpretations of XPS spectra of nickel metal and oxides. *Surf. Sci.* **2006**, *600*, 1771–1779. [CrossRef]
60. McWilliams, C.R.; Celinska, J.; de Araujo, C.A.P.; Xue, K.-H. Device characterization of correlated electron random access memories. *J. Appl. Phys.* **2011**, *109*, 091608. [CrossRef]
61. Kwon, D.-H.; Lee, S.R.; Choi, Y.S.; Son, S.-B.; Oh, K.H.; Char, K.; Kim, M. Observation of the Ni2 O3 phase in a NiO thin-film resistive switching system. *Phys. Status Solidi (RRL)–Rapid Res. Lett.* **2017**, *11*, 1700048. [CrossRef]